CONSTRUCTION AND OPERATION OF A TEST RFQ LINAC FOR HEAVY IONS

T. NAKANISHI, N. UEDA, S. ARAI, T. HATTORI,† T. FUKUSHIMA,
Y. SAKURADA,‡ T. HONMA, N. TOKUDA, S. YAMADA,
A. MIZOBUCHI, and Y. HIRAO

Institute for Nuclear Study, University of Tokyo, Midori-Cho 3–2–1, Tanashi-Shi, Tokyo 188, Japan

and

A. ITANO and M. TAKANAKA

National Institute of Radiological Sciences, Anagawa, Chiba 260, Japan

The INS radio-frequency quadrupole (RFQ) linac LITL (Lithium Ion Test Linac), a four-vane structure driven at 100 MHz by a single loop coupler, has been constructed. A field uniformity with an error of ±1% has been obtained by using capacitive end tuners and inductive side tuners. An unloaded Q value of 11,000, 60% of the ideal value, has been obtained. Beam dynamics has been studied by means of a formulation of the potential function for the radial matching section and for a method of rapid bunching. Ion beams such as H^+, H_2^+, $^3He^+$, and $^{6,7}Li^+$ are injected at 5 keV/amu and accelerated up to 138 keV/amu through the vane length of 1.22 m. The results of the beam tests agree with computer simulations with PARMTEQ, and the techniques developed in this work have been validated.

1. INTRODUCTION

Radio-frequency quadrupole (RFQ) linacs based on the proposal of Kapchinskii and Teplyakov (K–T)[1] have been developed at many laboratories since the success of the proof-of-principle (POP) machine at the Los Alamos National Laboratory (LANL).[2] At the Institute for Nuclear Study (INS) of the University of Tokyo, a 100 MHz heavy-ion RFQ linac (LITL) has been constructed to pursue the possibility of its application to the first stage of the injector for a heavy-ion synchrotron. This RFQ successfully accelerated ions with a charge-to-mass ratio larger than 1/7, following the acceleration of proton beams at the Institute of High-Energy Physics (IHEP)[3] and LANL.

The LITL has a four-vane structure in which the TE210 mode is generated. The merits of a four-vane cavity are several: (i) The structure is simple and strong, (ii) cooling of the structure is easy, (iii) a high Q value is expected, and

---

† Present address: Nuclear Reactor Laboratory, Tokyo Institute of Technology, Ohokayama 2, Meguro-ku, Tokyo 152, Japan.

‡ Present address: ULVAC Corporation, 2500 Hagisono, Chigasaki, Kanagawa 253, Japan.

(iv) the resonant frequency is predictable with the computer code SUPERFISH. There were, however, subjects to be studied on mode separation and field distribution. The TE110 mode, which generates a dipole field, lies close to the required TE210 mode because of heavy capacitive loading between the vanes. The TE111 and the TE211 mode also approach the TE210 mode as the ratio of cavity length to diameter increases. The mixing of the TE210 and these modes distorts the field distribution. Besides, positioning errors of the vanes strongly affect the field distribution. Moreover, mechanical asymmetry of the four chambers due to a coupler to feed rf power might affect the field distribution.

The 425-MHz POP cavity at LANL was driven by a coaxial manifold having a symmetrical and multislot coupling to maintain the symmetry of the four chambers.[4] On the other hand, a single loop coupler was applied at INS for the following reasons: (i) The cavity diameter is smaller, (ii) cooling and the mechanical structure is simpler, (iii) rf power dissipation is lower, (iv) impedance matching for effective power feed into the cavity is accomplished easily by rotating the coupling loop.

To pursue the feasibility of a loop coupler, low-power tests were done using two model cavities.[5] The model study showed that the required field distribution is attainable with a loop coupler. A method of mounting the vanes accurately to a cavity-cylinder with good rf contact was also assured in the fabrication of the second model. On the basis of the model study, the test RFQ LITL, driven at 100 MHz, was constructed; the cavity diameter is 56 cm, and the vane length is 122 cm. As for the beam dynamics design, a potential function in the radial matching section was formulated, and a design method for the vane parameters was developed to attain a rapid bunching. The performance of the cavity was studied in lower-power and high-power tests. Subsequently, beam tests were performed by accelerating ions, such as H^+, H_2^+, $^3He^+$, and $^{6,7}Li^+$, up to 138 keV/amu.

This paper describes the beam dynamics design, the cavity construction, the rf tests, and the beam tests of the LITL.

2. BEAM DYNAMICS DESIGN

2.1. *Operation Conditions of the LITL*

The LITL was designed to accelerate ions with a charge-to-mass ratio ε, larger than 1/7. Though it is possible to design a 200-MHz RFQ with a practical acceptance $\gtrsim 0.5\pi$ mm · mrad normalized, the operating frequency was chosen at 100 MHz for the following reasons: (i) A combination of the RFQ and a 100-MHz drift tube linac would be preferable as a system for acceleration of heavy ions with medium mass number; (ii) the diameter of the cavity is around 60 cm, and the fabrication is relatively easy; and (iii) the shunt impedance is higher than that of a 200-MHz RFQ. The maximum vane surface field of 20.5 MV/m (1.8 Kilpatrick) was supposed to be applicable. Considering ion sources and their related power supplies available at INS, the input beam parameters were chosen as listed in Table I, where the results of the beam dynamics design are also listed.

TABLE I

Principal Parameters of the LITL

Charge-to-mass ratio, ε	$\geq 1/7$
Operating frequency (MHz)	100
Input energy (keV/amu)	5
Output energy (keV/amu)	138
Normalized emittance, ε_n (mm · mrad)	$0.6\,\pi$
Cavity length (cm)	138
Cavity diameter (cm)	56
Vane length (cm)	122
Total number of cells	132
Characteristic bore radius, r_0 (cm)	0.41
Minimum bore radius, α_{min} (cm)	0.25
Margin of bore radius, $\alpha_{min}/\alpha_{beam}$	1.10
Maximum modulation, m_{max}	2.2
Focusing strength, B_0	5.0
Maximum defocusing strength, Δ_b	-0.110
Synchronous phase, ϕ_s (deg)	$-90 \rightarrow -30$
Intervane voltage for $\varepsilon = 1/7$ (kV)	61.8
Maximum field (MV/m)	20.5 (1.8 Kilpat.)
Power dissipation for $\varepsilon = 1/7$ (kW)	22 (exp.)
Transmission (designed) (%)	(0 emA input) 94
	(2 emA input) 92
	(10 emA input) 74

2.2. Principle of Beam Dynamics Design

In a low-current heavy-ion RFQ, such as the LITL, space-charge effects are not as important as in a proton or a deuteron RFQ. Therefore, we were able to develop a beam dynamics design emphasizing rapid bunching and high acceleration rates. To do so, we programmed a computer code GENRFQ,[6] a generator of the vane parameters for PARMTEQ. Our method was different from those of K–T[1] and LANL,[7] which are suitable for high-intensity beams. In the K–T method, the beam is bunched with a constant longitudinal charge density; this is realized with two invariant quantities, the frequency of small-amplitude phase oscillation and the spatial bunch length. The former invariant leads to a constant rf defocusing parameter. As the synchronous phase ϕ_s starts from $-90°$, the constant Δ_{rf} results in a slow increase of the synchronous phase and particle velocity; consequently, a long bunching section is required. The K–T method was generalized at LANL and improved by shortening the section by gradually decreasing the phase oscillation frequency and increasing the bunch length.

In the GENRFQ method, the RFQ is divided into six sections. As shown in Table II, in each section except for the radial matching section, physical constraints are imposed on three of six parameters: the aperture parameter α, ϕ_s, the modulation parameter m, the focusing parameter B, Δ_{rf}, and a separatrix parameter S. The parameter S is proportional to the product of the phase width

TABLE II

Constraints on Parameters in the GENRFQ Design

	Radical Matching	Shaper	Prebuncher	Buncher	Booster	Accelerator
α	—	—	—	—	—	α_{min}
ϕ_s	—	$-90° \to -88°$	$-60°$		$-30°$	$-30°$
m	—	—	—	—	—	—
B	$B_0 \sin k'z$	B_0	B_0	B_0	B_0	B_0
Δ_{rf}	—	$0 \to R_\Delta \Delta_b$	$R_\Delta \Delta_b \to \Delta_b$	Δ_b	Δ_b	—
S	—	—	S_0	S_0	—	—

Parameters for which no values are shown are dependent parameters.

and the height of the separatrix, as defined later by Eq. (5). Consequently, the vane geometry is determined for each cell. The RFQ parameters of the LITL are graphically shown in Fig. 1 as a function of cell number.

In the radial matching section, B increases sinusoidally from zero to its final value B_0, which is an invariant in the rest of the RFQ. The derivation of the sinusoidally increasing B is to be described in Section 2.5, and the optimization procedure for B_0 in Section 2.3.

In the shaper, a separatrix is formed by varying ϕ_s from $-90°$ to $-88°$, and Δ_{rf} from zero to $R_\Delta \Delta_b$ proportionally to axial distance. The quantity Δ_b is the value of Δ_{rf} at the output of the following prebuncher. The length of the shaper, R_Δ, and Δ_b are input parameters to GENRFQ. The procedure used to obtain adequate values of R_Δ and Δ_b is to be described in Section 2.4.
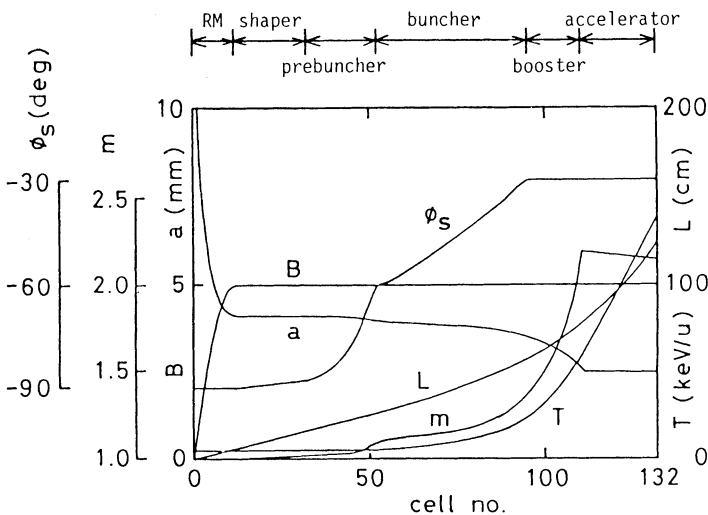

FIGURE 1   Vane parameters for the LITL as a function of cell number.

In the prebuncher, the quantity S is kept constant at S_0, the value at the output of the shaper. The defocusing parameter Δ_{rf} is decreased to Δ_b—the absolute value increases—as a function of the beam velocity so that the synchronous phase reaches $-60°$ at the output of this section, and the number of small-amplitude phase oscillation is 0.5. The synchronous phase is quickly increased, as shown in Fig. 1. The procedure of the rapid bunching is to be described in detail later.

In the buncher, the synchronous phase is increased to its final value, $-30°$ at the LITL, with $B = B_0$, $\Delta_{rf} = \Delta_b$, and $S = S_0$.

In the booster, $B = B_0$, $\Delta_{rf} = \Delta_b$, and $\phi_s = -30°$. The modulation parameter m increases steeply to its maximum value; as a result, the aperture α decreases rapidly. This section terminates when α reaches its final value α_{min}, set at a value slightly larger than the beam radius.

The accelerator section continues with $B = B_0$, $\phi_s = -30°$, and $\alpha = \alpha_{min}$ until the energy reaches its final value.

2.3. Choice of B_0 and Δ_b

Setting B_0 and Δ_b at adequate values is important to obtain high acceleration rates and a high transmission efficiency. These parameters are inputs to GENRFQ, and their optimized values should be searched for by examining the PARMTEQ results. However, their rough values, around which the optimization should be done, are set once the following quantities are given: charge-to-mass ratio, operating frequency, normalized emittance, and maximum surface field.

In the accelerator section, α is kept constant at α_{min}, slightly larger than the beam radius:

$$\alpha_{min} = f_\varepsilon [(\varepsilon_n \lambda / \pi) \Gamma_+ (B_0, \Delta_b)]^{1/2}, \tag{1}$$

where f_ε is a safety factor, 1.1 at the LITL, ε_n the normalized emittance, and Γ_+ the ratio of the maximum of the betatron function to the focusing period ($\Gamma_+ = \beta_{max}/\beta\lambda$). The smooth approximation solution for Γ_+ is

$$\Gamma_+(B, \Delta) = \left(1 + \frac{B}{4\pi^2}\right)^2 \left(\Delta + \frac{B^2}{8\pi^2}\right)^{-1/2}. \tag{2}$$

A new dimensionless parameter Y is introduced;

$$Y = \left(\frac{q\lambda E_s}{Mc^2\kappa}\right)^2 \frac{\pi\lambda}{\varepsilon_n}, \tag{3}$$

where E_s is the maximum surface field on a vane tip and $\kappa = E_s/(V/r_0)$, 1.36 for our vane's geometry. With the parameter Y and the focusing efficiency X,

$$X = \frac{I_0(k\alpha) + I_0(mk\alpha)}{m^2 I_0(k\alpha) + I_0(mk\alpha)}, \tag{4}$$
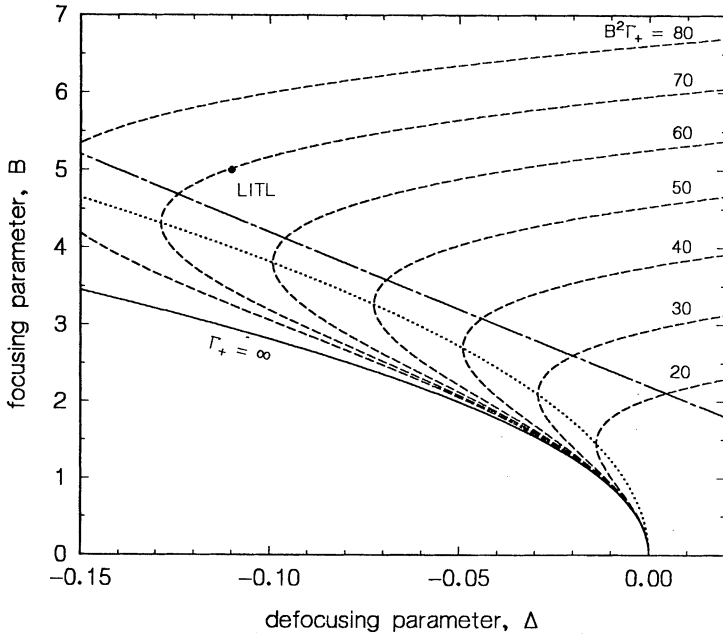
with

$$k = 2\pi/\beta\lambda, \tag{5}$$

FIGURE 2   Contour lines of constant $B^2\Gamma_+$ (dashed lines). On the dotted line, $\partial(B^2\Gamma_+)/\partial B = 0$. An optimum operation point for B_0 and Δ_b lies in the vicinity of the dash-dotted line, $B = 2.2 - 20\,|\Delta|$; $B_0 = 5$ and $\Delta_b = -0.11$ for the LITL.

Eq. (1) leads to

$$\frac{YX}{f_\varepsilon^2} = B^2\Gamma_+(B, \Delta). \tag{6}$$

Contour lines for constant $B^2\Gamma_+$, derived from Eq. (2), are drawn with dashed lines in the Δ–B plane in Fig. 2; on the dotted line in the figure, $\partial(B^2\Gamma_+)/\partial B = 0$. If a definite value of X in Eq. (6) is given, the operating point might be chosen at a crossing point of the dashed line and the dotted one, where $|\Delta_b|$ takes the maximum value and a high acceleration rate is attained. Empirically, however, a slightly larger value of B is preferable to obtain a higher transmission efficiency; the operating point lies near $B = 2.2 - 20\,|\Delta|$, the dash-dotted line in Fig. 2. Instead of a definite X, which is unavailable before the parameter optimization with GENRFQ and PARMTEQ, a rough value can be estimated. As X is approximately given by $X \simeq 2/(m^2 + 1)$, X is expected to be ~0.3–0.4 for m around 2. Thus, a rough value of $B^2\Gamma_+$ is obtained, and the operating point is searched for in the vicinity of the $B = 2.2 - 20\,|\Delta|$ line. At the LITL, the resulting values are $B_0 = 5$ and $\Delta_b = -0.11$.

2.4. Bunching Procedure in the Prebuncher

In the prebuncher, the synchronous phase is increased from $-88°$ to $-60°$ during a half period of small-amplitude phase oscillation for a constant separatrix

parameter S. This parameter is proportional to the product of the separatrix width and the height and is defined by

$$S = \sqrt{|\Delta_{rf}|}\, \beta^2 g(\phi_s), \tag{7}$$

$$g(\phi_s) = (\Phi/2\pi)(1 - \phi_s \cot \phi_s)^{1/2}, \tag{8}$$

where $\beta = v/c$, and Φ is the phase width of the separatrix. The parameter Δ_{rf} in Eq. (7) varies from Δ_1 to Δ_b as a function of the particle velocity:

$$\Delta = \Delta_b f(\xi), \tag{9}$$

with

$$f(\xi) = 1 - (1 - R_\Delta)\left(\frac{\xi - R_\beta}{1 - R_\beta}\right)^n. \tag{10}$$

Here, the velocity increases from β_1 to β_2, $\xi = \beta/\beta_1$, $R_\Delta = \Delta_1/\Delta_b$, $R_\beta = \beta_2/\beta_1$, and n is a positive integer, chosen as 2 in the LITL design. The condition of constant S leads to a relation between R_β and R_Δ:

$$R_\Delta = \left(\frac{g(-60°)}{g(-88°)}\right)^2 R_\beta^4. \tag{11}$$

For a given value of Δ_b, an adequate value of R_β is derived from the limit imposed on the number of small-amplitude phase oscillations (SAPO). This number is calculated with

$$N_{SAPO} = \frac{1}{2\sqrt{|\Delta_b|}} \int_1^{R_\beta} \frac{|\tan \phi_s|}{f^{1/2}(\xi)} \frac{d\xi}{\xi}. \tag{12}$$

The integral is numerically calculated, to search for the value of R_β that yields $N_{SAPO} = 0.5$.

2.5. Potential function in the Radial Matching Section

For the potential function in the radial matching section, we use

$$U(r, \psi, z) = \frac{V}{2} \frac{I_2(k'r)}{I_2(k'\alpha)} \sin k'z \cos 2\psi, \tag{13}$$

$$k' = \pi/2l. \tag{14}$$

In these equations, I_2 is a modified Bessel function of second order, V the intervane voltage, α the bore radius at the exist of the section, and l the length of the section. This potential function is derived from a general expansion of a Fourier–Bessel series by imposing boundary conditions that the potential is zero on the beam axis and the cavity end wall.[8] The radial component of the electric field is almost linear in the beam region, and the resulting focusing parameter increases sinusoidally with axial distance:

$$B(z) = B_0 \sin k'z. \tag{15}$$

At the LITL, $B_0 = 5$ and $l = 6\beta\lambda$, or 5.9 cm.

The computer code PARMTEQ was modified to trace particles in the radial matching section. In the calculation, the effect of the longitudinal component of the electric field is considered. Through the radial matching section of the LITL, the energy spread increases from zero to 3% (full width); this is too small to affect the longitudinal capture of the beam.

2.6. Results and Discussions of Beam Dynamics Design

The resulting RFQ parameters of the LITL are listed in Table I and shown graphically in Fig. 1. Simulated beam profiles, generated with the aid of the OUTPROC code, are shown in Figs. 3(a)–(c). As is apparent in Figs. 3(b) and (c), the envelopes of the phase and energy profiles are close to the separatrix during the bunching process. This results from the rapid bunching method used to increase the synchronous phase and the modulation. On the other hand, our bunching method is not effective in obtaining a high transmission efficiency for a
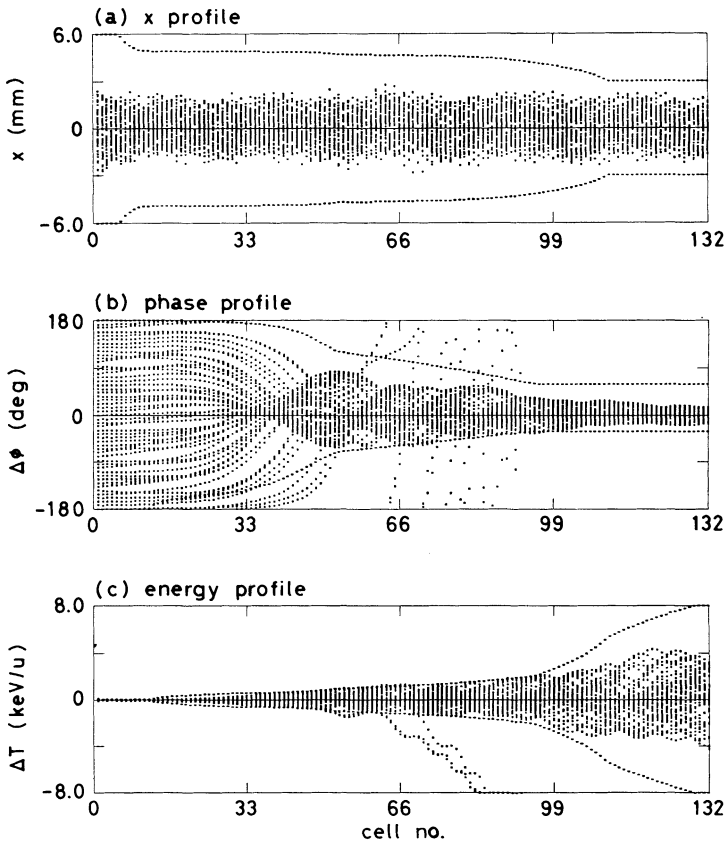

FIGURE 3   Simulated beam profiles in the LITL: (a) *x* profile, (b) phase profile, and (c) energy profile.

high-current beam. The designed transmission efficiency is 94% neglecting space-charge effects; for an input current of about 25 emA ($\varepsilon = 1/7$) or higher, the output is limited to 9 emA. Considering the present technology of ion sources, this current limit is sufficiently high for a heavy-ion RFQ, except for a special case, namely, applications to heavy-ion fusion, for which high-current singly charged ions must be accelerated. Therefore, the GENRFQ method is suitable for the design of a low-intensity heavy-ion RFQ.

The lengths and current limits of machines designed with our method and the LANL method are notably different. As an example, we compare 200-MHz Ne^{5+} machines with a 1-MeV/amu output energy.[6] For the GENRFQ machine, the length is 3.3 m, and the output current is 8 emA for a 10 emA input; whereas, for the LANL machine,[9] the corresponding numbers are 4.2 m and 9 emA. For 200-MHz O^{6+} machines of 140 keV/amu,[10] the length and the current limit are, respectively, 86 cm and 4.5 emA with our method, 131 cm and 9.3 emA with the LANL method.

The parameter Y is useful for evaluating the feasibility of designing an RFQ for a certain operating condition, defined by the parameters in Eq. (3): charge-to-mass ratio, normalized emittance, Kilpatrick factor, and operating frequency. At the LITL, Y is 235, and the modulation parameter has its maximum value m_{max} of 2.2 at the input of the accelerator section. The acceleration voltage per unit length also takes its maximum value of 1.5 MV/m at the input, whereas it decreases to 1.0 MV/m at the output. The fact that the value of m_{max} exceeds 2 results from the large Y. If the operating frequency is set at 200 MHz instead of our 100 MHz, Y decreases significantly to 50. For this case, we tried designing a machine with a zero-current transmission efficiency around 90%; the result shows that m_{max} is around 1.5 and that the maximum acceleration voltage is about 1 MV/m. According to experience, a value of Y smaller than 50 makes it difficult to design an RFQ with a zero-current transmission efficiency higher than 90%.

3. CAVITY CONSTRUCTION

3.1. Structure

An inside view and a schematic drawing of the LITL are shown in Figs. 4 and 5, respectively. The cavity cylinder is 0.56 m in diameter, 1.38 m in length, and 35 mm in thickness. It is made of mild steel, and its inner wall is plated with copper to a thickness of 0.2 mm. The wall thickness of 35 mm is required to drill holes for bolt holes and locater pins for vane mounting (see Fig. 6), and is thick enough to resist deflection: The calculated deflection of a 20-mm-thick cylinder with the vanes is 9 μm. Copper tubes of 10 mm diameter for water cooling are soldered on the outer wall of the cavity cylinder.

The vanes are made of oxygen-free copper. Each vane is mounted to the cavity cylinder using four cylindrical plugs (vane mounting plugs), as shown in Fig. 6. The vanes contact the cavity cylinder electrically by means of stainless-steel tubes of a 2.4 mm diameter, with a 0.1-mm silver coating.
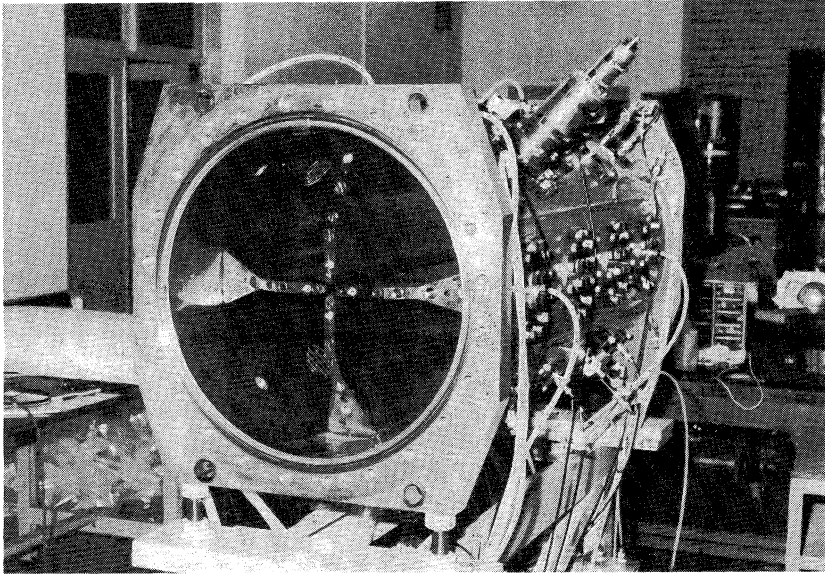
FIGURE 4   The LITL, viewed from the input side.

Vane extenders are attached to both ends of the vanes. To allow the magnetic flux return, the end area (the trapezoidal area in Fig. 5) is about a half of the cross-sectional area of a quadrant. The vane extenders are demountable, in case machining is required for tuning the rf field. A test using a cold model indicated that the end areas should be broadened by cutting the vane extenders in the case where the field distribution is tuned with capacitive end tuners set against the
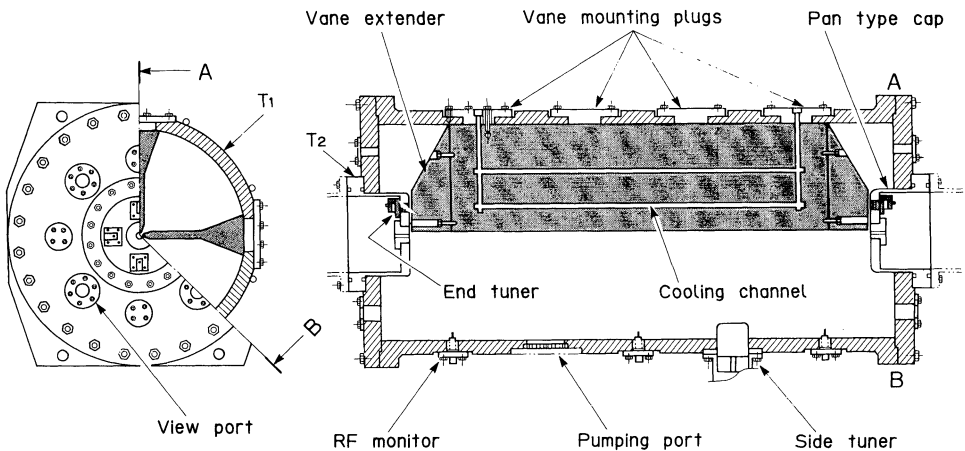
FIGURE 5   Schematic drawing of the LITL structure. Temperature was measured at positions T_1 and T_2 for the high-power test described in Section 4.5.
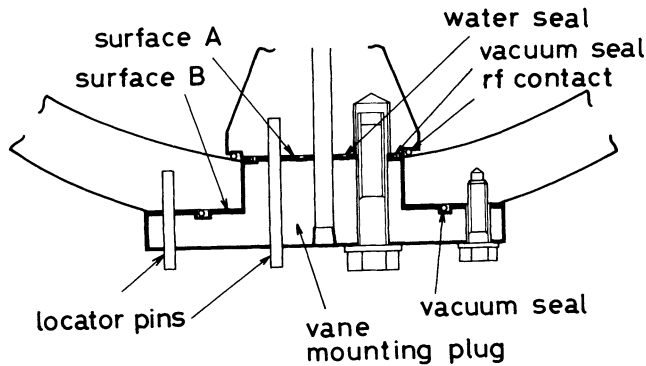
FIGURE 6 Schematic showing the method of vane mounting to the cavity cylinder, using the vane mounting plug.

vanes, with gaps narrower than about half of the vane-to-vane gap. For the LITL cavity, however, the machining of the vane extenders was not necessary, because the tuned gaps between the tuners and the vanes were sufficiently broad. At the high-energy side, the output ends of the vane extenders are truncated without any special treatment at $kz = \pi$, that is, at the top or the bottom of the modulation.

End plates of mild steel, with view ports, were copper plated. Pan-type caps are attached to the end plates, facing the vane ends, because long vane extenders increase current density at the vane-to-cylinder joints near the ends of the vanes. The caps are made of copper, except for the flange. Finger contactors are used for rf contact between the caps and the end plates. The end plates and the caps are not cooled by water.

The goal for the surface smoothness of the cavity cylinder and the vanes was determined to be less than 1.6 S, considering the skin depth to be 6.6 μm at 100 MHz. Here, S denotes a unit for surface roughness: 1.6 S means the maximum cusp height on a surface is 1.6 μm. The measured surface roughness is 0.8 S for the cavity cylinder and 2–3 S for the vanes.

The cavity is driven by a single loop coupler located near the longitudinal center. The coupler is rotatable for easy impedance matching. The required rf power is 22 kW for cw acceleration of ions with $\varepsilon = 1/7$. The loop is cooled indirectly since the outer conductor of the coupler system is water-cooled near the loop. An inductive side tuner of a plunger type is installed in each of the quadrants. These tuners, 85 mm in diameter, are made of aluminum alloy and are movable over a stroke of 50 mm with pulsed motors. Four capacitive end tuners are mounted to each of the pan-type caps. Each of the quadrants has three monitoring loops.

The cavity is evacuated with a turbomolecular pump with a capacity of 500 l/s. A copper grid is attached at the interface between the cavity cylinder and the pumping port to prevent leakage of rf power. The effective pumping speed at the grid is calculated to be 130 l/s. The measured pressure at the cavity end wall is 6×10^{-7} Torr during operation with a beam.

3.2. Vane Machining

The vane-tip shape to produce the exact RFQ field is derived from the potential function given by K–T:[1]

$$r^2 \cos 2\psi = \frac{\alpha^2}{1 - AI_0(k\alpha)} [1 - AI_0(kr) \cos kz], \tag{16}$$

where

$$A = \frac{m^2 - 1}{m^2 I_0(k\alpha) + I_0(mk\alpha)}, \tag{17}$$

$$k = 2\pi/\beta\lambda. \tag{18}$$

The parameters α and m are defined in Fig. 7, and I_0 is a modified Bessel function of zeroth order. At the LITL, however, the vane-tip shape in the transverse plane is approximated by a circular arc with a radius of curvature derived from Eq. (16) by setting $\psi = 0$ or $\pi/2$ (see Fig. 7). This shape gives wider vane-to-vane gaps, and as a result, a higher intervane voltage can be applied. The transverse cross section of the vanes and the cavity cylinder was designed using the program SUPERFISH so that the resonant frequency was 100 MHz for the TE210 mode. The vane-tip shape in the radial matching section is also approximated by a circular arc.

A numerically controlled (NC) mill for the vane-tip machining has a 1.8-m-long bed. The carbide ball-end mill is 5 mm in radius; the vane radius of curvature takes its minimum value of 5.5 mm near the output of the prebuncher section. The vanes were finally cut at a 0.5-mm increment along the longitudinal axis after three steps of rough cuts at 2-mm increments. The spindle speed was 2000 rpm.
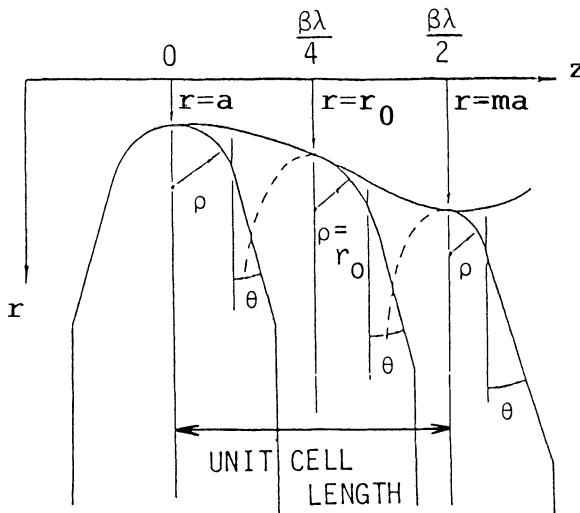

FIGURE 7   Vane tip geometry; $\theta = 15°$.

Errors of machining by the NC mill were measured with a three-dimensional coordinate measuring machine with an accuracy of 5 μm and were within ±30 μm over the whole vane length of 1.22 m.

After the NC machining, the vanes were electropolished by 30 μm to make the surfaces smooth. The surface roughness on the vane top and the side wall was measured in the direction of the rf current; the resulting value was less than 2 S. As for the vane top, the roughness in the longitudinal direction was tested with a small unmodulated vane machined under the same condition as the real vanes. The result showed that a roughness of 7 S after the NC machining was reduced to 3 S with the electropolishing.

3.3. Cavity Cylinder Plating

Cyanide copper plating was adopted for the cavity cylinder. Prior to the LITL fabrication, the electrical quality of cyanide copper plating was tested by measuring Q values with two small cylindrical resonators. They are 120 mm in length and 144 mm in diameter and have a resonant frequency of 2013 MHz for the TM010 mode. One resonator was made of solid copper, and the other was made of mild steel, plated with copper to a 24 μm thickness, except for the end plates of solid copper. The measured Q values for the two resonators were almost equal, about 25,200, corresponding to 95% of the calculated value for an ideal solid-copper cavity.

The plating of the LITL cavity cylinder is based on this experience. Table III summarizes the plating process. Before the plating, the surface to be plated was buffed to a roughness of 3 S for good plating. For uniform plating of a 200-μm total thickness, the plating process was divided into three stages [(9), (10), and (13) in Table III]: (i) 20-μm-thick copper strike, (ii) 150-μm plating, and (iii) 30-μm plating after a check of the thickness. In each plating process, care for uniform plating was taken: the cavity cylinder was rotated, and the polarity of the electrodes was periodically reversed in the ratio of five for plating copper to one for removing it. In the process of the plating, the surfaces for the vane mounting plugs were masked against plating.

The final surface roughness measured 0.8 S. Before the vane mounting, Q values were measured for various modes and were 80–90% of those for an ideal cylindrical resonator. For example, the measured value was 65,700 for the TM010 mode, compared with the SUPERFISH value of 74,600. For the measurement, all ports on the cylinder were closed with blank flanges.

3.4. Vane Mounting and Alignment

First, without rf contactors and vacuum seals, the four vanes, except for the vane extenders, were temporarily mounted to the cylinder with the vane mounting plugs. Then the cavity was placed on a surface plate so that one of the horizontal vanes was parallel to the plate. Heights of the reference points on the opposite

TABLE III

Copper Plating Process

(1) Alkali degreasing	
(2) Water rinsing	
(3) Derusting	
Solution: HCl	~10–15%
Temperature:	~25°C
Time:	15 min
(4) Water rinsing	
(5) Neutralizing	
Counteractive: NaCN	~3–5%
(6) Water rinsing	
(7) Electrolytic degreasing	
Solution: NaCN	50 g/l
Temperature:	~30–50°C
Time:	~3–5 min
(8) Water rinsing	
(9) Copper striking	
Solution: CuCN	~20–35 g/l
KCN	~37–60 g/l
Current density:	0.02 A/cm^2
Temperature:	50°C
Time:	50 min
Thickness:	20 μm
(10) Copper plating	
Solution: CuCN	~50–70 g/l
KCN	~82–120 g/l
additions	~74–118 g/l
Current density:	0.01 A/cm^2
Temperature:	~50–65°C
Time:	6.25 hours
Thickness:	150 μm
(11) Water rinsing	
(12) Buffing	
(13) Check of thickness	
(14) Copper plating	
Time:	1.25 hours
Thickness:	30 μm
(15) Water rinsing	
(16) Chromate bathing	
Solution: CrO$_3$	50 g/l
H$_2$SO$_4$	5 g/l
(17) Water rinsing	
(18) Drying	

vane were measured; as a result, the vane was adjusted to be horizontal. The heights of the tips of the vertical vanes were measured to determine the amount by which surface A or B (see Fig. 6) should be machined to correct the radial positions of the vane tips. These measurements were done at both the vane ends. Then the cavity was rotated by 90° to repeat the procedure.

With the machined plugs, the vanes were aligned longitudinally and trans-

versely by using clearances between the plugs and the cylinder. After the vane tips were positioned to an accuracy of ±0.1 mm, holes for locator pins were drilled through the plugs into the vanes and the cavity cylinder. The cavity was disassembled and cleaned. Then the vanes, mounted with rf contactors, the vacuum and water seals, and the vane extenders were attached. The vane positioning with the locator pins was reproducible with high accuracy.

4. RF ASPECTS OF THE CAVITY

4.1. Mode Measurement

Figure 8 shows rf field levels in the four quadrants after field tuning. They are shown as a function of the input signal as it is swept from 99 to 103 MHz. Two TE110 modes exist near the required TE210 mode; the nearer TE110 has a resonant frequency 1.3 MHz higher than the TE210 frequency of 99.8 MHz. Resonant frequencies for higher modes are 153.8 MHz for TE211 and 151.8 and 152.3 MHz for TE111. As this RFQ cavity has a small length-to-diameter ratio, the TE211 and the TE111 mode have frequencies so much higher than the TE210 mode that they do not affect the required field distribution.
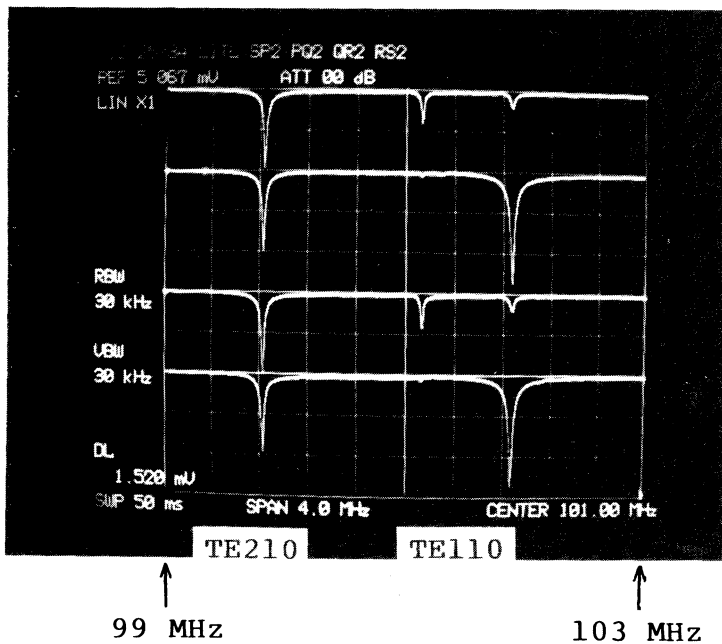

FIGURE 8   Resonance curves for the four quadrants of the LITL; frequency was swept from 99 to 103 MHz.

4.2. Field Distribution

Figure 9 shows magnetic field distributions before and after field tuning with the end tuners. The magnetic field was sensed with the monitoring loops installed at three places in each quadrant. The coupling factors of the loops were adjusted to within ±0.7% of one another. As shown in the figure, the levels at both ends are about 20% lower than those at the center. This is caused by leakage of magnetic flux to the adjacent quadrants at the cavity ends, which decreases flux densities at the quadrants' azimuthal centers, where the loops are installed. During this measurement, the longitudinal distribution of electric field in the vane-to-vane gap was flat, as shown later.
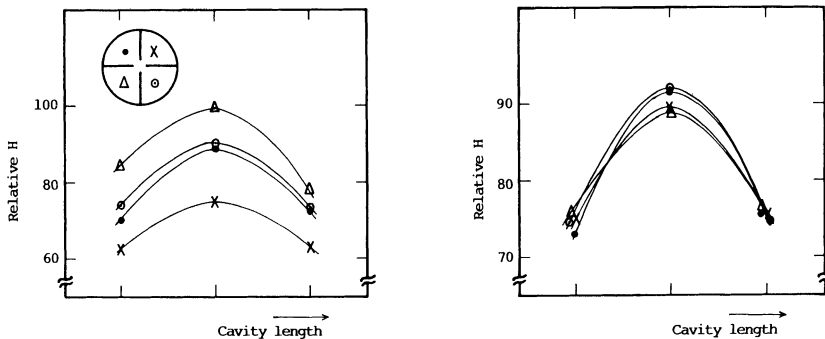

FIGURE 9   Magnetic field distributions in the LITL, measured with the monitoring loops: (a) before and (b) after field tuning. The longitudinal positions of the loops are shown in Fig. 5.

Azimuthal electric field balance among the four vane-to-vane gaps was finally checked by a perturbation method using a thick dielectric thread, which was stretched over the length of the cavity at the transverse positions shown in Fig. 10. The azimuthal field imbalance was small (less than ±2%, which was further reduced to ±1% by using the side tuners).

Longitudinal distributions of the electric field were measured with a perturbation method. A field perturber (a table tennis ball) was moved with a pulsed
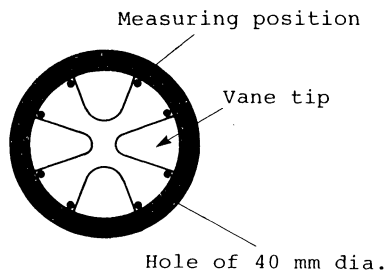

FIGURE 10   Setting positions of a thick thread for the measurements of the azimuthal electric field distribution.
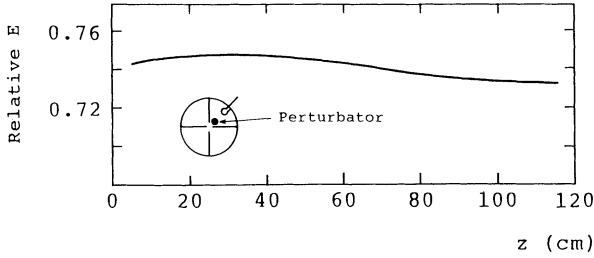
FIGURE 11   Longitudinal distribution of the electric field in the vane-to-vane gap.

motor, using the vanes as a guide. An example for one quadrant is shown in Fig. 11. The distributions in the other quadrants are almost identical. The longitudinal distribution is flat to within ±1%. The minimum gap between the end tuners and the vanes is 2.45 mm; the surface field is 12.6 MV/m, or 1.1 Kilpatrick.

4.3. Effects of Side Tuners

The four side tuners are used to compensate a shift of resonant frequency due to variations of temperature. Simultaneous insertion of the four tuners increases the resonant frequency by 6.2 kHz/mm over the full stroke of 50 mm. This frequency tuning does not disturb the azimuthal field balance, even when the initial depths of the tuners are different.

   The side tuners are also used for adjusting the field distribution. Insertion of a side tuner into a quadrant decreases its field level by 0.2%/mm over the full stroke and increases the one in the opposite quadrant by the same amount; however, neither the field levels in the adjacent quadrants nor the longitudinal voltage distribution is affected. It should be noted that these effects are peculiar to a four-vane cavity with a small length-to-diameter ratio, such as the LITL cavity.

4.4. Impedance Matching

The input impedance of the cavity is matched easily to the characteristic impedance of the rf feeder line by rotating the coupling loop. The voltage reflection coefficient is less than 0.01 at resonance. The coupling loop has an effective area of 23 cm^2 with a loop area of 43 cm^2 for the impedance matching. The value estimated from an equivalent circuit analysis is 27 cm^2. The required area A of a loop is given by

$$A = S\left[\frac{4}{Q_0}\frac{L_i}{L_0}\left(\frac{R_c}{\omega L_i} + \frac{\omega L_i}{R_c}\right)\right]^{1/2}, \tag{19}$$

where S is the cross-sectional area of a quadrant, Q_0 is the unloaded Q value, L_0

is the inductance of a quadrant, L_i is the self-inductance of the loop, and R_c is the characteristic impedance of the rf feeder line.

The unloaded Q value measured 9500 just after cavity construction and improved to 11,000 after the high-power operation described below. The latter value corresponds to 60% of 17,900, which is the SUPERFISH value for an ideal infinitely long cavity.

4.5. High-Power Test

The rf power is supplied from a 25-kW system of a master oscillator and a power amplifier. The final tube is a tetrode EIMAC 4CW25000A. The power is fed into the cavity through a coaxial line WX-77D and the loop coupler.

The rf power in the cavity was measured with a monitoring loop at the cavity center. The coupling factor of the loop was calibrated by feeding a measured low power to the cavity under a condition of negligibly small reflection. The relation between the intervane voltage and rf power was determined by the beam test described in Section 5.2; a power of 22 kW corresponds to the design voltage of 62 kV for the acceleration of $^7Li^+$ ions. The required power agrees with a calculated value of 21.4 kW from the measured Q value and a stored energy evaluated by SUPERFISH.

After training of 5 hours, a maximum surface field strength of 20.5 kV/mm (1.8 Kilpatrick) was applied for a few minutes of cw operation. During pulse operation of 1-ms duration and 10-ms repetition period, field strengths up to 2 Kilpatrick were achieved stably.[11]

After the beam test, pits due to sparking were observed on the end walls, the capacitive tuners, and the cylinder wall near the coupler. A few pits were observed around the vane tips of the radial matching section. Dark stain was observed on the surfaces of the cutbacks of the vane extenders and on the cylinder wall opposite them.

When the cavity was excited at 7 kW cw, the frequency decreased from 99.56 MHz by 250 kHz during the first 10 minutes, as shown in Fig. 12, but the field balance among the quadrants did not change. The observed frequency shift is one order of magnitude larger than the expected value. First, we guessed that the shift is caused by narrowing of the gaps between the vane ends and the opposing walls. To investigate the dependence of frequency on gap distance, we measured frequency shift in atmospheric pressure by broadening the gaps at both cavity ends. Upon broadening the gaps by 1 mm, the frequency increased by 245 kHz. If this rate is applicable also for the case of narrowing of the gaps, the gaps should be narrower by 1 mm during high-power operation. This estimated value is unreasonably large.

A probable cause of the frequency shift is narrowing of the vane-to-vane gaps due to thermal expansion of the vanes and the cavity cylinder. According to a simple calculation,[11] the shift of −250 kHz can be attributed to a temperature increase of 30°C at the vanes. In this calculation, the expansion of the cavity cylinder caused by the observed temperature increase (T_1 in Fig. 5) is considered.
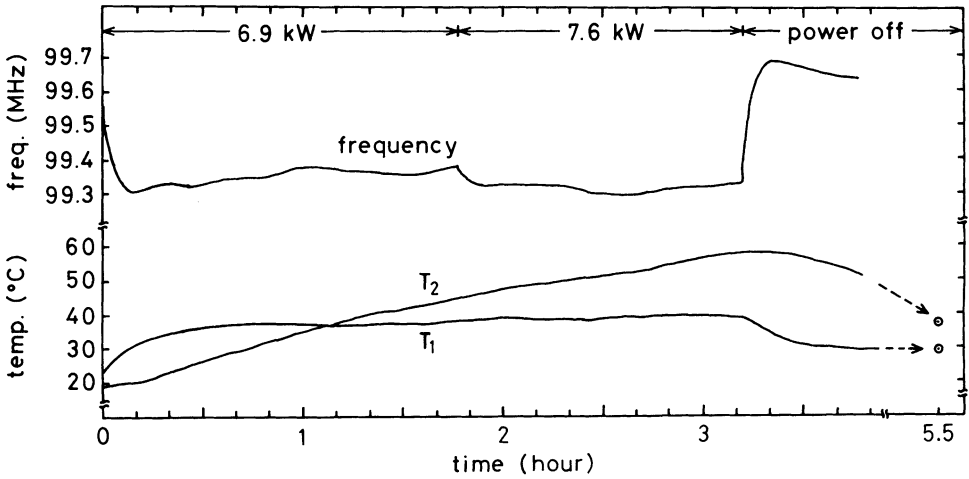
FIGURE 12   Time variation of the resonant frequency f, the temperature T_1 on the cavity side wall, and the temperature T_2 on the end wall during cw high-power operation around $7 \, kW$.

This estimated vane heating contradicts a result of a computer calculation, which predicts a temperature increase of less than 14°C, even during full-power operation. Nonetheless, this explanation seem probable if vane cooling is less effective than expected. This experience shows that the cooling of the vanes, including the vane extenders, should be improved.

5. BEAM TEST

5.1. Beam Test Stand

The layout of the beam test stand is shown in Fig. 13. The beam optics design was performed with the computer code MAGIC. A thin-lens approximation was used

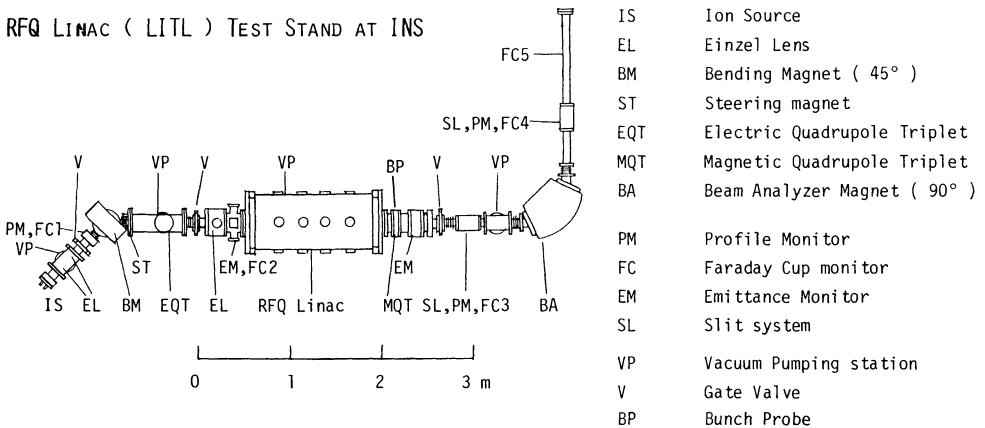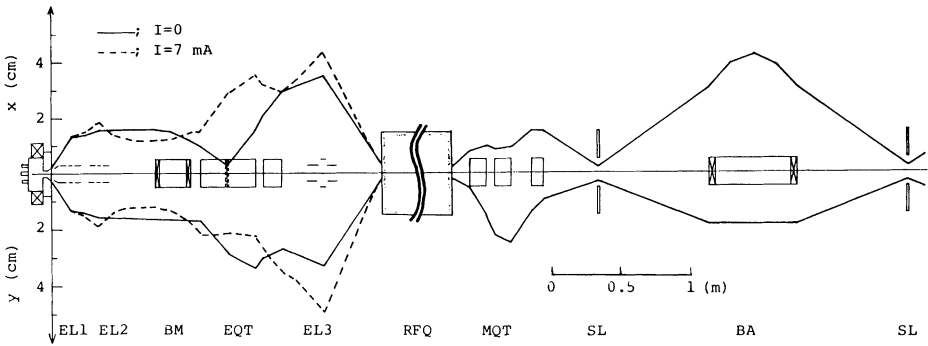|	
IS	Ion Source
EL	Einzel Lens
BM	Bending Magnet (45°)
ST	Steering magnet
EQT	Electric Quadrupole Triplet
MQT	Magnetic Quadrupole Triplet
BA	Beam Analyzer Magnet (90°)
PM	Profile Monitor
FC	Faraday Cup monitor
EM	Emittance Monitor
SL	Slit system
VP	Vacuum Pumping station
V	Gate Valve
BP	Bunch Probe

FIGURE 13   Layout of the beam test stand.

FIGURE 14   Beam envelopes in the beam test stand, calculated with MAGIC.

for the einzel lenses. The aberrations in einzel lenses and electric quadrupole lenses were ignored. The space-charge effect was approximated by thin lenses placed at intervals of about 10 cm. The resulting beam envelopes are shown in Fig. 14. At the entrance of the RFQ, the input beam is shaped to have a radius of 3 mm, and an angle $(\gamma\varepsilon/\pi)^{1/2}$ of 85 mrad.

A surface-ionization-type ion source was used for lithium ions. Singly charged lithium ions of 20 or 30 μA were extracted at 35 kV. For ions of gaseous materials, a duoplasmatron-type ion source was used at first and was then replaced by a microwave ion source. Ion beams of a few milliamps were extracted from these sources.

The extracted ion beam of 5 keV/amu is transported through two sets of einzel lenses to a separating magnet. The separated ion beam is then focused with a triplet of electric quadrupole lenses and an einzel lens so as to match the RFQ acceptance. The einzel lens has a high-voltage electrode 180 mm in diameter and two grounded ones of 100 mm. Such large diameters are required by the large envelope angle of the input beam. The intensity and the emittance of the input beam are measured with double slits and a Faraday cup behind the einzel lens. The second slit and the Faraday cup are placed 7 cm upstream from the entrance of the RFQ, that is, they are in the pan-type cap.

The accelerated beam is focused on the object point of an analyzer magnet with a triplet of quadrupole magnets. The quadrupole magnets have spiral plate coils and are compact enough to be placed near the exit of the RFQ. Considering the angle of 30 mrad of the output beam, this placement is advantageous to reduction of the bore radius; it is 25 mm, and the maximum field gradient is 3.2 kG/cm. The analyzer magnet has an orbit radius of 40 cm and a bending angle of 90°. The magnet has vertical focusing, with the edges inclined to the beam at 63.4°. The maximum field of 10.5 kG is at the full coil current of 630 A. The dispersion is 1.6 m at the image point. A defining slit system, a multiwire profile moinitor, and a Faraday cup are placed at both the object and the image points of the magnet.

5.2. Transmission Efficiency

Transmission efficiency was measured with a cw proton beam of $80 \mu A$. The horizontal and vertical emittance measured 150 and 120π mm · mrad, respectively, at the input of the RFQ. Their profiles are shown in Fig. 15. The ellipses in the figure are for 300π mm · mrad, or 0.98π mm · mrad normalized, and include the measured beam emittances. The output current was measured with the FC3 Faraday cup, placed at 0.5 m beyond the triplet quadrupole magnets. Despite the absence of an analyzer magnet, only accelerated protons are detected. Though unaccelerated protons might be transported through the RFQ, they diverge in the quadrupole magnets and do not reach the Faraday cup. At this place, the horizontal beta function is 0.05 m, and the vertical one is 0.14 m for a 138-keV/amu beam, whereas they are, respectively, 5100 and 34,000 m for a 5-keV/amu beam. Therefore, the number of protons that reach the Faraday cup is negligibly small.

Transmission efficiency was measured as a function of intervane voltage. In Fig. 16, the measured transmission efficiencies are plotted with dots; the solid line denotes the PARMTEQ result for accelerated protons, and the dashed line the result for unaccelerated protons. The abscissa represents the normalized intervane voltage V_n, defined by $V_n = 7\varepsilon V_{op}/V_0$, where ε is the charge-to-mass ratio, V_{op} is the intervane voltage at operation, and V_0 is 61.8 kV, the design value for $\varepsilon = 1/7$. It should be noted that the measured transmission efficiencies agree with the solid line at $V_n < 1$, but not with the dashed line. This means that unaccelerated protons do not reach the Faraday cup.

The measured transmission efficiency exceeds 90% in a range $1.4 < V_n < 2.3$, decreases steeply at $V_n > 3$, and vanishes at $V_n = 3.6$. This decrease is caused by
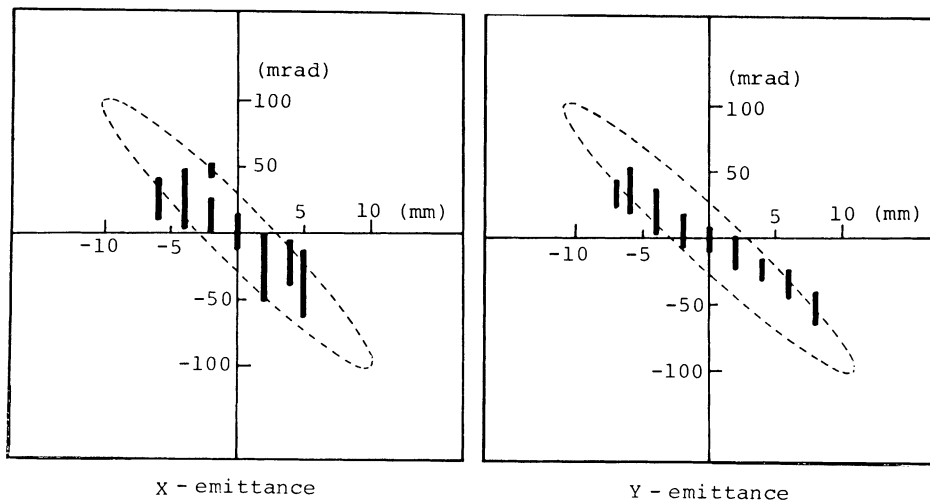

X – emittance   Y – emittance

FIGURE 15 Measured emittance of the input H^+ beam. The ellipses show the emittance of 300π mm · mrad, which is used in the simulation of the transmission shown in Fig. 16.
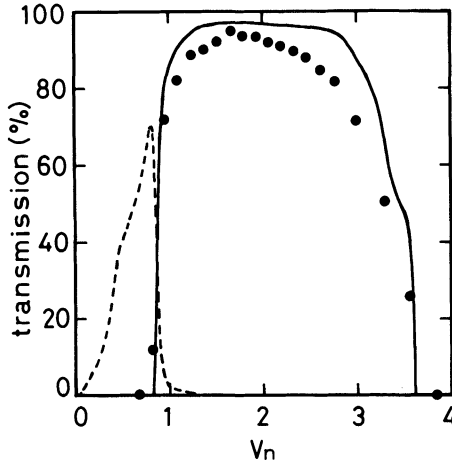
FIGURE 16   Transmission as a function of vane voltage for the proton beam. The solid curve shows the PARMTEQ result for accelerated protons, and the broken line the result for protons transported without acceleration.

the approach of the Δ–B operation point to the boundary where the phase advance per focusing period is π and where Γ_+ is infinity. At $V_n = 3.6$, the focusing parameter B is 18, and the point $(B, \Delta) = (17.9, 0)$ lies on the boundary; therefore, the transverse motion is unstable in the shaper section, where Δ_{rf} is nearly zero.

For $V_n < 1$, the transmission efficiency also decreases steeply. The explanation is as follows. As V_n decreases below 1, the synchronous phase, designed to be $-30°$ in the accelerator section, should approach $0°$ to keep the energy gain, that is, $V_n \cos \phi_s$, constant. When ϕ_s reaches $0°$ (at $V_n = 0.87$), the separatrix disappears, and the beam is not accelerated to the designed final energy. At $V_n = 0.87$, the PARMTEQ simulation also gives vanishing transmission. Therefore, we consider that for $V_n = 0.87$, or $V_{op} = 7.6$ kV, the transmission efficiency vanishes. By measuring the output voltage of the monitor loop at $V_n = 0.87$, the monitor loop was calibrated to obtain the applied intervane voltage.

5.3. Transverse Emittance of the Output Beam

The emittance of the output protons was measured 26 cm downstream from the exit of the RFQ. The quadrupole magnets between the RFQ and the emittance monitor were not excited. Figure 17 shows the experimental result (bars), in comparison with the computer simulation (dots). The emittance of the output beam is about $40\,\pi$ mm · mrad, $0.7\,\pi$ mm · mrad normalized, for both the x and the y emittance. The agreement between experiment and simulation means that the vane truncation at the output end has little effect on the beam.
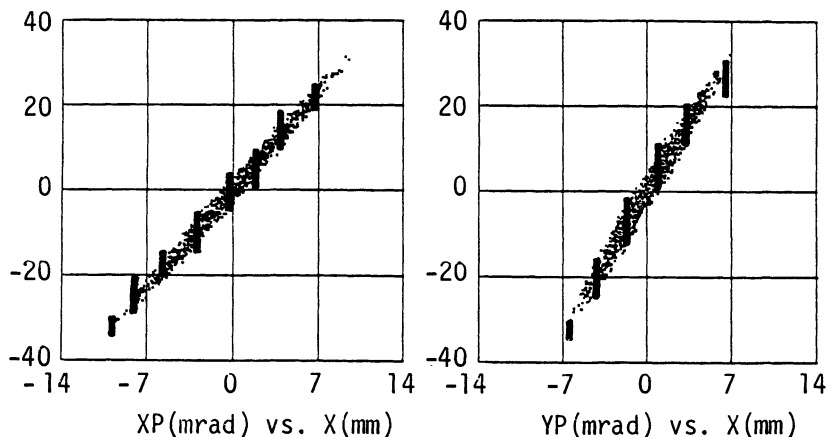
FIGURE 17   Measured emittances of the output H^+ beam (bars) and PARMTEQ results (dots).

5.4. Energy of the Output Beam

The momentum of the output beam was measured with a resolution of 0.25% full width by using the analyzer magnet. The momentum spectra for H^+, H_2^+, and $^3He^+$ beams are shown in Fig. 18, and those for $^6Li^+$, and $^7Li^+$ beams are in Fig. 19. The intervane voltage is set at $V_n = 1$. From the coil currents, the energies at the peaks were determined to be 137.6 ± 3.5 keV/amu. The momentum spread is about 2% FWHM. For these measurements, the cavity was operated cw for the H^+ and H_2^+ beams, and in a pulsed mode (2-ms pulse width, 35% duty factor), for the other heavy-ions beams.
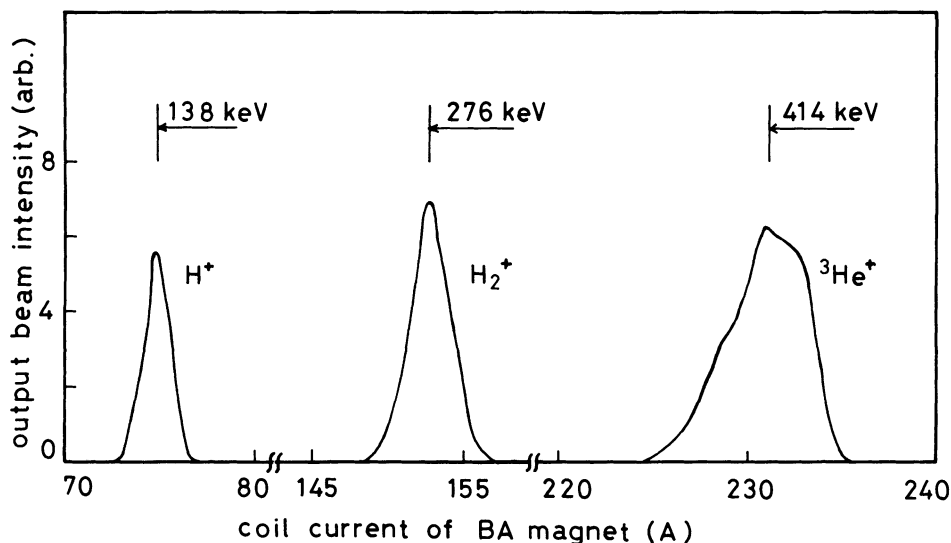

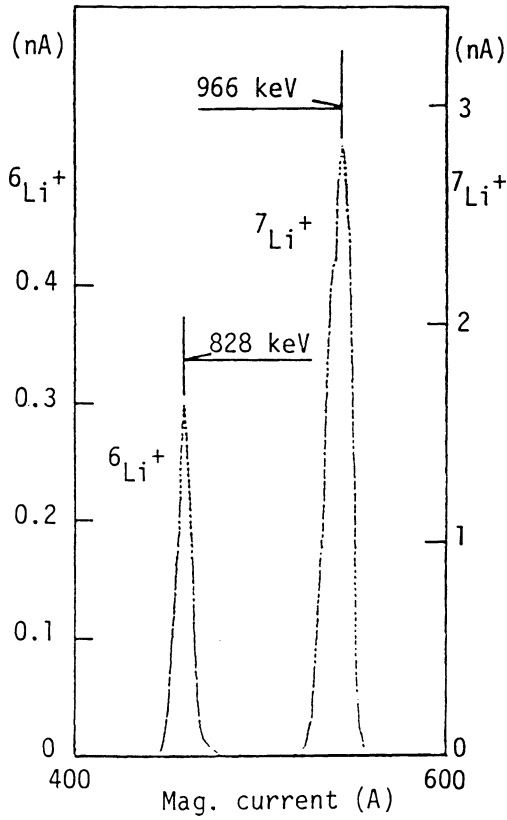FIGURE 18   Momentum spectra for H^+, H_2^+, and $^3He^+$ beams.

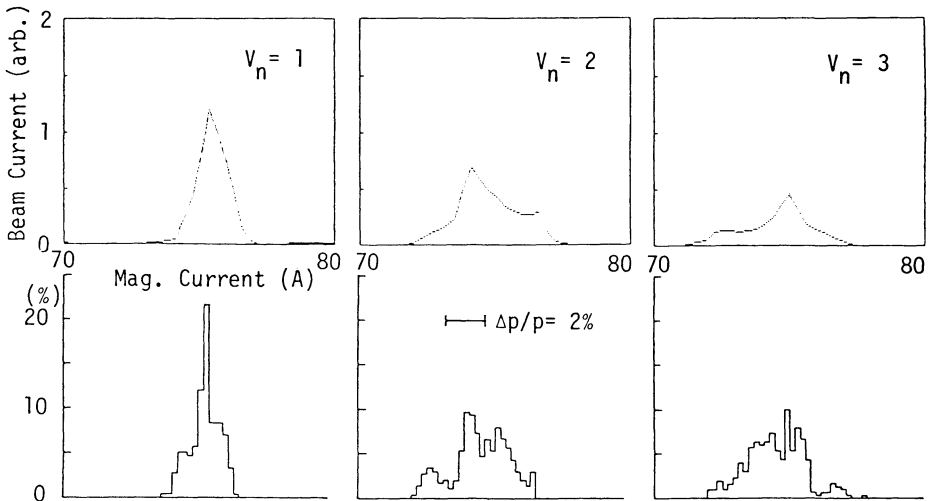FIGURE 19   Momentum spectra for $^6Li^+$ and $^7Li^+$ beams.

FIGURE 20   Momentum spreads for the proton beam at $V_n = 1, 2, 3$; the measured results are shown below the respective computer simulations.

The momentum spectrum of a H^+ beam was measured by varying the intervane voltage. In Fig. 20, the experimental results are compared with the computer simulation. The momentum spread at $V_n = 2$ is 1.7 times broader than that at $V_n = 1$. The measured widths agree with the simulation.

5.5. Bunch Length of the Output Beam

The bunch structure of the output beam was observed with a bunch probe placed 26 cm away from the RFQ exist. The probe head is made of a tantalum disk 20 mm in diameter enclosed in a copper housing. A mesh of fine tungsten wires is
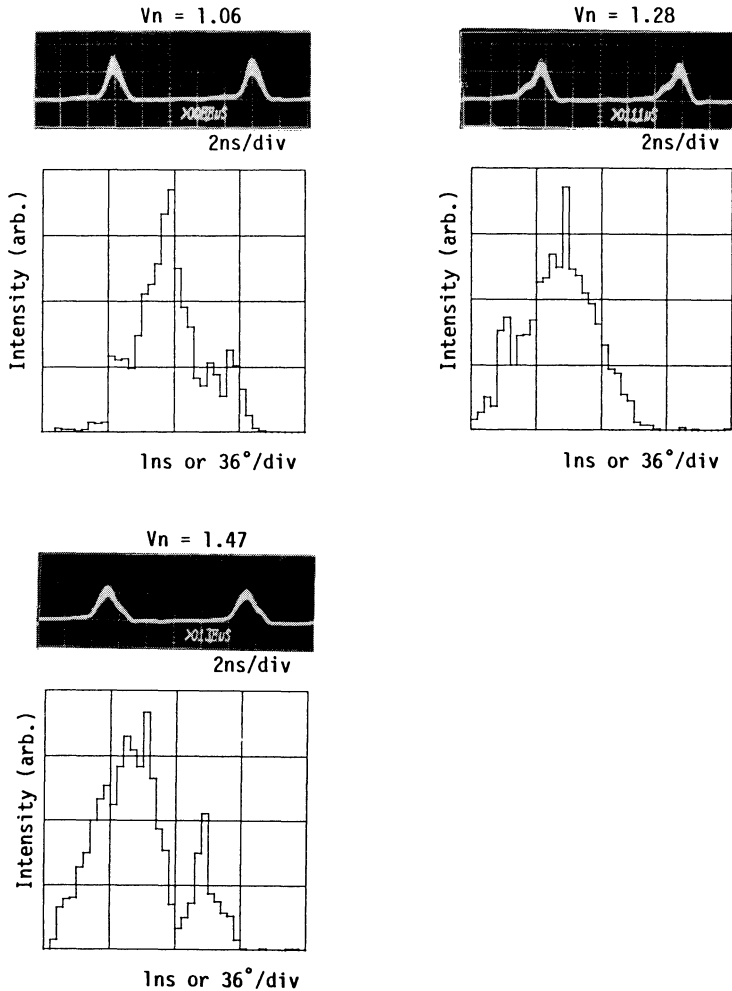

FIGURE 21   Time structure of the output H_2^+ beam at $V_n = 1.06$, 1.28, and 1.47.

placed in front of the disk, and a voltage of about -200 V is applied to the mesh. The mesh suppresses secondary electrons emitted from the disk by ion bombardment and gives sharp bunch signals. The characteristic impedance of the probe is $50\,\Omega$. The attenuation in the probe and the coaxial cable to a 1 GHz oscilloscope was measured to be 5% at 1 GHz.

In Fig. 21, the time structure of a H_2^+ beam is given for three values of the intervane voltage, $V_n = 1.06$, 1.28, and 1.47. The FWHM width at $V_n = 1.06$ is $40°$, or 1 ns, which agrees with the simulation. The observed bunch width at $V_n = 1.06$ is two times broader than one at the exit of the RFQ because of the flight path of 26 cm.

6. CONCLUSION

Our techniques for the fabrication and tuning of the RFQ cavity were validated by the results on rf characteristics. The vane-mounting method with the plugs resulted in vane alignment with a tolerance of ± 0.1 mm, and the vane-to-cylinder contact produced a Q value of 11,000, 60% of the ideal value. We had no trouble field tuning the cavity, driven with a single loop coupler. With the capacitive end tuners, a field uniformity was obtained to within $\pm 2\%$, which was further improved to $\pm 1\%$ by using the inductive side tuners. The problem left to be solved is unstable operation at high power; the observed abrupt frequency shift of -250 kHz during 7-kW cw operation, 30% of full power, showed that the cooling of the vanes should be improved.

The results of the beam test agreed with the PARMTEQ simulation. This success established the feasibility of the methods employed: the GENRFQ method, including the new radial matching section; the circular approximation of the vane tip; and the truncation of the vanes at the output end.

The techniques developed in this work have been applied to a long RFQ (TALL), an extended version of the LITL. The study with the TALL RFQ has started. During the first beam test, protons and molecular hydrogen were accelerated to the design energy of 800 keV/amu through the 7.25-m-long machine.

Works, Toshiba Corporation; the authors thank engineers there for their collaboration during this work. Calculations with GENRFQ, PARMTEQ, MAGIC, SUPERFISH, etc., were performed on a FACOM M 380 at the INS Computer Room.

REFERENCES

1. I. M. Kapchinskij and V. A. Teplyakov, *Prib. Tekh. Eksp.* **19,** 19 (1970).
2. J. E. Stovall *et al., Proc. 6th Conf. on the Application of Accelerators in Research and Industry,* Denton, TX, 1980.
3. B. M. Gorshkov *et al., Sov. Phys. Tech. Phys.* **22,** 1348 (1977).
4. J. M. Potter, *Proc. 1979 Linear Accelerator Conf.,* Montauk, NY, p. 138.
5. T. Nakanishi *et al.,* INS technical report INS-NUMA-30 (1982).
6. S. Yamada, *Proc. 1981 Linear Accelerator Conf.,* Santa Fe, NM, p. 316.
7. K. R. Crandall *et al., Proc. 1979 Linear Accelerator Conf.,* Montauk, NY, p. 205.
8. N. Tokuda and Y. Yamada, *Proc. 4th Symp. on Accelerators and Technology,* RIKEN, Wako, Saitama, Japan, 1982, p. 105.
9. T. P. Wangler and R. H. Stokes, *Proc. 6th Conf. on the Applications of Accelerators in Research and Industry,* Denton, TX, 1980.
10. J. Staples, *Proc. 1984 INS Intern. Symp. on Heavy Ion Accelerators and their Applications to Inertial Fusion,* INS, Tokyo, Japan, 1984, p. 379.
11. N. Tokuda, *Proc. High-Current, High-Brightness, and High-Duty-Factor Ion Injectors Workshop,* San Diego, CA, May 1985. AIP Conference Series (to be published).